Environmental Science & Technology

Open Access

pubs.acs.org/est

Article

Enhanced Manganese Oxidation at the Biofilm−Fluid Interface Drives Pore-Scale Patterns in Mineral Precipitation

Eleanor C. Fadely, Gaitan Gehin, Sharon E. Bone, Samuel M. Webb, Verónica L. Morales, and Jasquelin Peña*

Cite This: *Environ. Sci. Technol.* 2026, 60, 654−663

Read Online

ACCESS | Metrics & More | Article Recommendations | Supporting Information

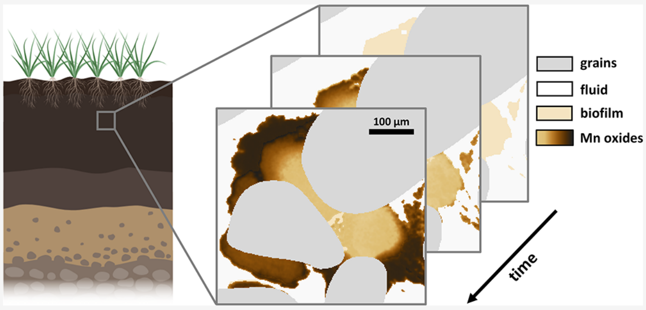

ABSTRACT: Microbial oxidation of manganese (Mn) from aqueous Mn(II) to solid-phase Mn(III, IV) minerals catalyzes Mn(II) removal in natural and engineered porous systems. However, little is known about the spatiotemporal evolution of Mn biomineralization in confined spaces that experience simultaneous Mn(II) delivery and Mn oxide precipitation. Here, we combine time-lapse microscopy, image analysis, and mass spectrometry to quantify the extent and rate of Mn biomineralization by *Pseudomonas putida* GB-1 in an optically transparent two-dimensional porous medium. We found that Mn(II) oxidation initially occurred within biofilms but shifted over time toward the edges of biofilms in contact with pore fluid. Minerals precipitated outside of the initial biofilm footprint likely due to surface-mediated oxidation of Mn(II) by nascent biogenic Mn oxides, reinforcing a gradient in mineral accumulation from the Mn(II) source near the reactor inlet to the outlet. The rate of mineral precipitation outside the biofilm footprint surpassed the rate of mineral accumulation inside biofilms within 6 h and accounted for two-thirds of the total Mn oxide mass in the pore space at the end of the experiment. This work advances a mechanistic understanding of coupled biotic and abiotic Mn oxidation in porous environments while providing a novel platform to quantify microbe−mineral−fluid interactions.

KEYWORDS: *manganese biomineralization, porous media, biofilms, microfluidics, heterogeneity*

1. INTRODUCTION

Bacteria and fungi drive the oxidative branch of the Mn cycle by oxidizing aqueous Mn(II) to Mn(III, IV) species.[1−3] The nanoparticulate minerals that form through this biomineralization reaction oxidize and stabilize organic matter,[4] sorb cationic metals,[5−10] and degrade contaminants.[11] Manganese-oxidizing microorganisms and their associated biominerals are widespread in soils, freshwater and marine sediments, and engineered treatment systems.[1,2,12−14] Typically, biogenic Mn oxides accumulate adjacent to cell surfaces and on extracellular polymeric substances (EPS), forming microbe-mineral assemblages[15,16] that can enhance the reactive capacity of both natural and engineered porous media. For instance, biogenic Mn oxides can interact with aqueous Mn(II), facilitating further abiotic Mn oxidation and subsequent mineral accumulation.[17,18] The mechanism of mineral precipitation, whether biotic, abiotic, or a combination thereof, has important implications for the extent and rate of mineral precipitation, as well as the reactivity of the resulting minerals toward other chemical species. However, quantitative and mechanistic knowledge of Mn oxide precipitation in soils and sediments is scarce.

Soils and sediments are inherently complex environments, containing pores of varying size and connectivity that induce preferential fluid flow[19] and nonuniform reactant transport.[20,21] This results in a heterogeneous distribution of microbes and geochemical species, which can enhance localized biogeochemical reactivity.[21−23] In these environments, biogenic Mn oxides occur as both particles and coatings on grain surfaces,[24] often accumulating along interfaces where microbes experience dynamic reactant (e.g., Mn, O_2) delivery.[25,26] However, the kinetics and mechanisms of Mn biomineralization within soil pore spaces cannot be derived without direct and real-time observation of mineral precipitation.

Some insights into Mn oxide precipitation in porous media are provided by studies of Mn removal in water treatment systems. These systems include column biofilters,[27−30] fixed-

Received: August 15, 2025
Revised: December 1, 2025
Accepted: December 3, 2025
Published: December 19, 2025

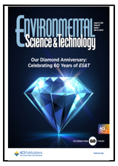

https://doi.org/10.1021/acs.est.5c11326

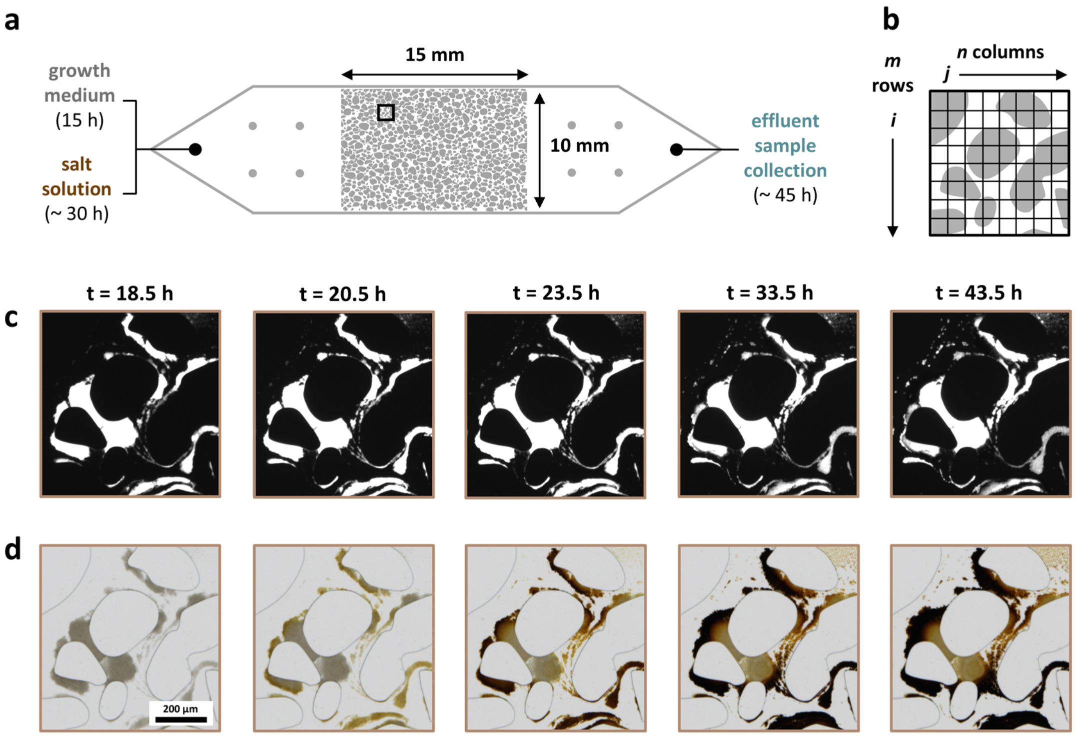

Figure 1. Experimental design and representative optical images. (a) Microfluidic reactor geometry (grains in gray and pore space in white) showing the input of the growth medium (t = 0 h to t = 15 h) and Mn-supplemented salt solution (t = 15 h to t = 43.5 h) at the reactor inlet and effluent sample collection at the reactor outlet (t = 0 h to t = 43.5 h). The black box within the pore space represents the detailed region shown in (b−d). (b) Schematic of matrix notation used to calculate biofilm growth and Mn oxide mass from segmented images (gridlines not to scale). (c) Contrast-adjusted fluorescence images of *P. putida* GB-1 biofilms in the pore space at select time points, as indicated by the bright areas in the images. Grains and pores without any biofilms appear in black. (d) Color brightfield images of *P. putida* GB-1 biofilms showing the accumulation of Mn oxide precipitates at select time points. Scale bar is 200 μm.

bed bioreactors,[31] and gravity-driven membranes[32] containing biofilms that precipitate Mn oxides in response to continuous Mn(II) input. Pore fluid and filter medium samples collected from sand-packed columns at discrete time points show that Mn(II) removal and Mn oxide precipitation are spatially nonuniform, becoming localized to the top half of the column following system start-up.[27,28,30] While microbial Mn oxidation is widely observed in these treatment systems,[27−32] chemical analysis of mature filter media[29,32] and assays of microbial viability[30] suggest that Mn(II) sorption and autocatalytic Mn oxidation also contribute to long-term Mn(II) removal. However, current methods cannot resolve the relative contribution of these processes to mineral precipitation and Mn(II) removal. A real-time and pore-scale analysis is therefore needed to evaluate the distribution, timing, and kinetics of biotic and abiotic Mn oxidation and thus gain a predictive understanding of mineral precipitation and reactivity in natural and engineered settings.

The aim of this work is to identify mechanisms that control the extent and rate of Mn biomineralization in porous media. To this end, we developed a novel microfluidic platform to simultaneously (i) measure ex situ removal of Mn(II) from reactor effluent using inductively coupled plasma mass spectrometry (ICP-MS) and (ii) visualize in situ biofilm formation and mineral accumulation with optical microscopy. Quantitative image analysis revealed that preferential mineral precipitation near the Mn(II) source was driven by localized accumulation of Mn oxides at the biofilm−fluid interface. The distinct timing and rates of Mn oxide precipitation relative to the initial biofilm footprint indicated a transition from enzymatic to surface-mediated Mn oxidation. Our study is the first to evaluate the spatiotemporal drivers of Mn biomineralization in situ and in real time. These findings enhance our understanding of Mn oxidation in soil environments and inform the development of engineered systems for contaminant removal.

2. MATERIALS AND METHODS

2.1. Bacterial Strain, Solution Chemistry, and Cell Culture. We used *Pseudomonas putida* GB-1 to quantify the in situ extent and rate of Mn biomineralization. *P. putida* GB-1 is an aerobic, biofilm-forming bacterium with two multicopper oxidase enzymes known to catalyze oxidative precipitation of Mn(III, IV) oxide minerals during the stationary phase of growth.[33,34] It has been widely used as a model organism for Mn oxidation,[2,3] and Mn-oxidizing strains of *Pseudomonas* have been identified in both natural and engineered porous environments.[2,3,14,35] To facilitate image segmentation, we selected a *P. putida* GB-1 strain with a constitutive mCherry fluorescent tag on the pTac promoter region. Detailed characterization of the growth of the fluorescent-tagged strain relative to the wild-type is provided in Figure S1 and Supporting Information Method S1.

The growth medium used to propagate *P. putida* GB-1 was adapted from Gehin et al.[33] as follows: 0.4 mM $CaCl_2{\cdot}2H_2O$, 0.25 mM $MgSO_4{\cdot}H_2O$, 0.25 mM Na_2HPO_4, 0.15 mM KH_2PO_4, 1:2 Fe(III)-EDTA (20 μM $FeCl_3{\cdot}6H_2O$ and 40 μM EDTA adjusted to pH 6.5), 10 mM HEPES buffer (adjusted to pH 7.0), 5 mM $(NH_4)_2SO_4$, 40 nM $CuSO_4{\cdot}5H_2O$, 273 nM $ZnSO_4{\cdot}7H_2O$, 84 nM $CoCl_2{\cdot}6H_2O$, 53.7 nM

$NaMoO_4 \cdot 2H_2O$, 1.5 g L^{-1} yeast extract, 1.5 g L^{-1} casamino acid, and 50 μM $MnCl_2 \cdot 4H_2O$ in sterile ultrapure water (Milli-Q, Millipore). All chemicals were of American Chemical Society (ACS) reagent grade or bacteriological grade, and all stock solutions were filter-sterilized with a 0.22 μm filter (PES, Fisher Scientific). A salt solution was prepared following the same recipe but excluding yeast extract, casamino acid, and Mn(II).

To culture bacterial cells, *P. putida* GB-1 was streaked from −80 °C glycerol stocks onto agar plates (2.5% Luria Broth Base or LB, 1.5% bacteriological agar) supplemented with 20 μg mL^{-1} gentamicin (Gm^{20}) and incubated at 30 °C overnight. A liquid preculture was prepared by adding one plate colony to 10 mL of 2.5% liquid LB supplemented with Gm^{20} and incubated in a 50 mL conical tube for 16 h at 30 °C and 180 rpm. After 16 h, a 1 mL aliquot of cell suspension was washed three times in salt solution (1 min centrifugation at 8000 rcf). The washed cells were resuspended to an optical density (OD_{600}) = 0.01 in 20 mL growth medium without Mn(II) and incubated for 6 h in a 50 mL Erlenmeyer flask at 30 °C and 180 rpm to reach the mid-exponential phase (OD_{600} ∼ 1.7−1.9). An inoculum was then prepared by diluting an aliquot of the mid-exponential phase preculture in 2 mL of salt solution supplemented with 50 μM Mn(II) to an initial OD_{600} = 0.005.

2.2. In Situ Bacterial Growth and Mn Biomineralization. We conducted microfluidic experiments in two phases. The first phase was used to establish Mn-oxidizing biofilms, which comprise surface-attached matrices of bacterial cells immobilized in EPS,[36] in the microfluidic reactor (hereafter, growth phase). The second phase was used to quantify Mn oxide precipitation (hereafter, mineralization phase). The transition between the growth and mineralization phases of the experiment was initiated by switching from the carbon-rich growth medium to the carbon-deficient salt solution supplemented with 50 μM Mn(II). This change in influent solution chemistry facilitated the onset of the stationary phase, a necessary condition to induce bacterial Mn oxidation and mineral precipitation.[33]

To begin an experiment, a microfluidic reactor was fabricated to represent the porous media commonly found in engineered water treatment systems. We adapted a porous geometry from Wang et al.[37] with a porosity of ∼0.41, which was comparable to column-scale systems for microbial Mn(II) removal used by Breda et al.[30] and Haukelidsaeter et al.[28] Reactors had a pore volume of ∼2.3 μL and a total volume of ∼10.9 μL including the inlet and outlet regions (Figures 1a, S2, and Supporting Information Method S2). This reactor was saturated by injecting salt solution supplemented with 50 μM Mn(II) through the outlet tubing (see Supporting Information Method S2) until no air bubbles were present (typically about 200−300 μL). A *P. putida* GB-1 inoculum with OD_{600} = 0.005 was then drawn through the reactor inlet using a syringe pump at the reactor outlet (NE-4002X, New Era) and sterile 5 mL glass syringe (1000 Series PTFE Luer Lock, Hamilton) fitted with a sterile blunt-tip needle (21-gauge, Jensen Global) for 20 min at a flow rate of 8.33 μL min^{-1}.

After inoculation, the reactor remained in a state of no flow for 1 h to promote bacterial settling and attachment. The inlet inoculation tubing was then replaced with tubing connected to the fluid control system (see Supporting Information Method S3). Subsequently, growth medium was injected for 15 h at a Darcy velocity of 5 m d^{-1}, which corresponds to a volumetric flow rate of 1.33 μL min^{-1} or a residence time of 1.7 min per pore volume (growth phase; ∼500 elapsed pore volumes), followed by salt solution supplemented with 50 μM Mn(II) for approximately 28.5 h (mineralization phase; ∼1000 elapsed pore volumes). To mitigate unwanted biofilm growth in the reactor inlet and outlet regions during the experiment, we irradiated these areas with a stage-top ultraviolet-C light-emitting diode (UVC LED) array adapted from Ramos et al.[38] at t = 0 h for 5 min to inactivate any bacteria that became attached during inoculation, then the outlet only at t = 17.5 h for 5 min to inactivate sloughed biofilms (see Figure S3 and Supporting Information Method S4). This strategy allowed us to compare the Mn oxide mass in the pore space to the total Mn mass in the reactor digestate (see the next section). The entire experimental setup, including reactor, tubing, and influent solutions, was maintained at 30 °C for the duration of the experiment using a custom-built microscope incubator. Experiments were conducted in triplicate.

2.3. Effluent Sampling and Chemical Analysis. We collected volume fractions of the reactor effluent during the growth and mineralization phases to confirm mass closure (see Tables S1, S2, and Supporting Information Method S5) and quantify Mn(II) removal. Effluent samples were collected into 1.5 mL microcentrifuge tubes in cumulative intervals every 2 h during the growth phase (t = 0 h to t = 15 h) and every hour during the first 12 h of the mineralization phase (t = 15 h to t = 27 h), followed by samples at t = 29 h, t = 39 h, and t = 43.5 h (23 total time points). The samples were immediately centrifuged for 5 min at 16,000 rcf to pellet any bacteria present in the effluent. We then diluted 60 μL of the supernatant in 2.94 mL 1% HNO_3 and measured the aqueous Mn(II) concentration using ICP-MS (Agilent 7900). The ICP-MS was fitted with a quartz spray chamber, microMist concentric gas nebulizer, and nickel sample and skimmer cones and was operated at a constant flow rate of 1.0 L min^{-1} argon gas and 4.5 mL min^{-1} helium gas. The Mn limit of quantification, calculated as 3.3 times the detection limit,[39] was 0.04 μg L^{-1} or 0.67 nM.

At the end of the mineralization phase (after 43.5 h), we recovered all solid-phase, sorbed, and aqueous Mn within the pore space by injecting 1 mL of a 40 mM oxalic acid and 2% nitric acid solution into the reactor with a syringe pump and 5 mL glass syringe at a flow rate of 100 μL min^{-1}. We repeated this acid-digestion procedure with the outlet tubing to recover any Mn oxides precipitated by sloughed biofilms between the reactor outlet and effluent collection tube. Finally, we diluted 30 μL of each digestate in 2.97 mL of 1% HNO_3 and measured the total Mn with ICP-MS.

2.4. Microscopy and Image Analysis. Reactor imaging was conducted using a Nikon Ti2 Eclipse inverted epifluorescence microscope fitted with a Hamamatsu ORCA-Fusion digital CMOS camera, Lumencor LIDA light engine (for brightfield imaging), and Lumencor SOLA light engine (for fluorescence imaging). Using NIS Elements software, we acquired 16-bit images in color brightfield (5 ms illumination, red illumination at 97.58%, green illumination at 44.76%, and blue illumination at 100%) and mCherry fluorescence modes (excitation: 562 ± 20 nm, emission: 641.5 ± 37.5 nm, 5 ms exposure, 100% intensity) with a 4× objective (Plan Apo λD 4×/0.20, 1.62 μm $pixel^{-1}$) every hour during the growth phase and every 30 min during the mineralization phase. These illumination settings were selected to enhance the brightness and set the color balance using a test reactor containing Mn-oxidizing biofilms and biogenic Mn oxides. Each image was a stitched composite of the whole reactor pore space (5 × 4 images, 2304 × 2304 pixels per field of view, 1% overlap). We applied a shading correction during image acquisition to remove the quilting artifacts that arise from uneven illumination of the individual images. Subsequently, time-lapse files were converted from .nd2 format to 16-bit tagged image file format.

Fluorescence (Figure 1c) and color brightfield (Figure 1d) images were processed using custom MATLAB (2024b) scripts to quantify (i) biofilm formation, (ii) Mn oxide mass, and (iii) the rate of Mn oxide precipitation. Briefly, we generated a calibration curve to assign Mn oxide pixel intensity to a known Mn mass (see Figures S4 and S5, and Supporting Information Method S6). Mineral suspensions with varying masses of solid-phase Mn were imaged with both optical microscopy, using the same color brightfield imaging settings as the microfluidic experiments, and micro-X-ray-fluorescence (μ-XRF) at the Stanford Synchrotron Radiation Lightsource Beamline 2−3. These μ-XRF measurements were calibrated to units of mass per pixel using gravimetric $MnCl_2{\cdot}4H_2O$ standards and then correlated to color brightfield pixel intensity (units of a.u.). This allowed us to compute the Mn oxide mass at each pixel within the reactor pore space at every experimental time point (see Figures 1b, S6 and Supporting Information Method S7). This approach accounted only for solid-phase Mn oxides that appear as brown or black precipitates. Any Mn(II) sorbed onto the biofilms would be transparent to optical microscopy and therefore was estimated through ex situ measurements of the reactor effluent. Results are presented as the average and standard deviation of triplicate experiments unless otherwise noted.

3. RESULTS AND DISCUSSION

3.1. Distinct Biofilm-Mediated Processes Drive Mn(II) Removal. Aqueous Mn(II) removal observed in the reactor effluent (Figure 2a) can be mapped to distinct biogeochemical processes within the pore space (Figure 2b). During the biofilm growth phase (t = 0 h to t = 15 h) and first 3 h of the mineralization phase (t = 15 h to t = 18 h), we observed a small but gradual decrease in effluent Mn(II) that coincided with bacterial growth and biofilm formation. The effluent Mn(II) concentration decreased slowly from 55.69 ± 4.38 μM at t = 2 h to 46.25 ± 0.65 μM at t = 18 h (Figure 2a). This accounts for a ∼17% decrease in Mn(II) concentration relative to the initial measurement at t = 2 h. In this time interval, color brightfield and fluorescence images showed stochastic biofilm development throughout the reactor pore space (Figures S7a,b and S8).

A transitional period of 3.5 h followed the switch from the growth to the mineralization phase at t = 15 h. The biofilms continued to grow and move slightly as the influent fluid was exchanged (Figure 2b). By t = 18.5 h, the biofilms were fixed in place and reached a steady-state footprint as identified from brightfield images (Figure S9). Using the mCherry fluorescence, which selectively showed the microbial biomass, we calculated a projected area of 12.32 ± 2.06 mm^2 (see Supporting Information Method S7), which is equivalent to 21.66 ± 3.61% of the reactor pore space. After t = 18.5 h, the subtle increase in the total biofilm area (Figure 2b) was due to intensifying constitutive fluorescence at the stationary phase[40] rather than active biomass growth (Figure S9).

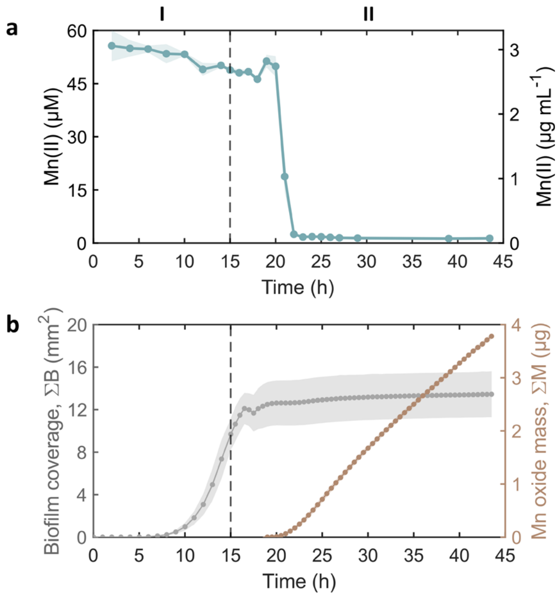

Figure 2. Global ex situ and in situ quantification of Mn biomineralization. The dashed line represents the fluid exchange initiating the transition from the growth (I, t = 0 h to t = 15 h) to the mineralization phase (II, t = 15 h to t = 43.5 h). (a) Drawdown of aqueous Mn(II) from the reactor effluent, as measured by ICP-MS. (b) Biofilm coverage (ΣB) calculated as the total sum of each binarized fluorescence image matrix (left axis) and cumulative Mn oxide mass (ΣM) calculated as the total sum of each calibrated color brightfield image matrix (right axis). Markers indicate the average of triplicate experiments, and shading indicates the standard deviation. For Mn oxide mass, markers are approximately the same size as the shaded uncertainty.

After t = 18.5 h, we observed rapid changes in the effluent Mn(II) concentration (Figure 2a) that coincided with the onset of Mn biomineralization (Figure 2b). Between t = 18 h and t = 19 h, the Mn(II) concentration increased slightly from 46.25 ± 0.65 μM to 51.33 ± 1.79 μM, followed by a steep decline from 49.87 ± 2.89 μM to 2.48 ± 0.28 μM between t = 20 h and t = 22 h. Prior to the onset of this rapid Mn(II) removal at t = 20 h, a total of 0.57 ± 0.16 μg Mn was retained in the microfluidic system. For the remainder of the experiment, we observed >95% removal of the influent Mn(II) (Table S2). Concurrent with Mn(II) removal, we observed a continuous increase in the mass of Mn oxides without reaching steady state (Figure 2b). At the final time point, we calculated a mass of 3.78 ± 0.05 μg Mn oxide within the reactor pore space (see Supporting Information Method S7), which matched the mass measured from the reactor digestate within 18% (Table S3). The moderate discrepancy between these two approaches suggests the presence of sorbed Mn(II) in the reactor pore space that is transparent to optical microscopy.

By comparing the timing of Mn(II) removal from the reactor effluent (Figure 2a) with the accumulation of solid-phase Mn in the reactor pore space (Figure 2b), we concluded that Mn oxide precipitation was preceded by the sorption of Mn(II) onto developing biofilms. Bacterial biomass and extracellular polymers within biofilms contain negatively charged or polar functional groups (e.g., carboxyl, phosphoryl, sulfhydryl) that facilitate adsorption of cationic metals, including Mn(II).[5,6,15,41−45] While intracellular accumulation of Mn(II) may have also contributed to the decrease in effluent Mn(II) during growth of *P. putida* GB-1, we expect Mn(II) absorption to be minimal relative to Mn(II) adsorption, based on the previous research using *P. putida* GB-1.[46] The small

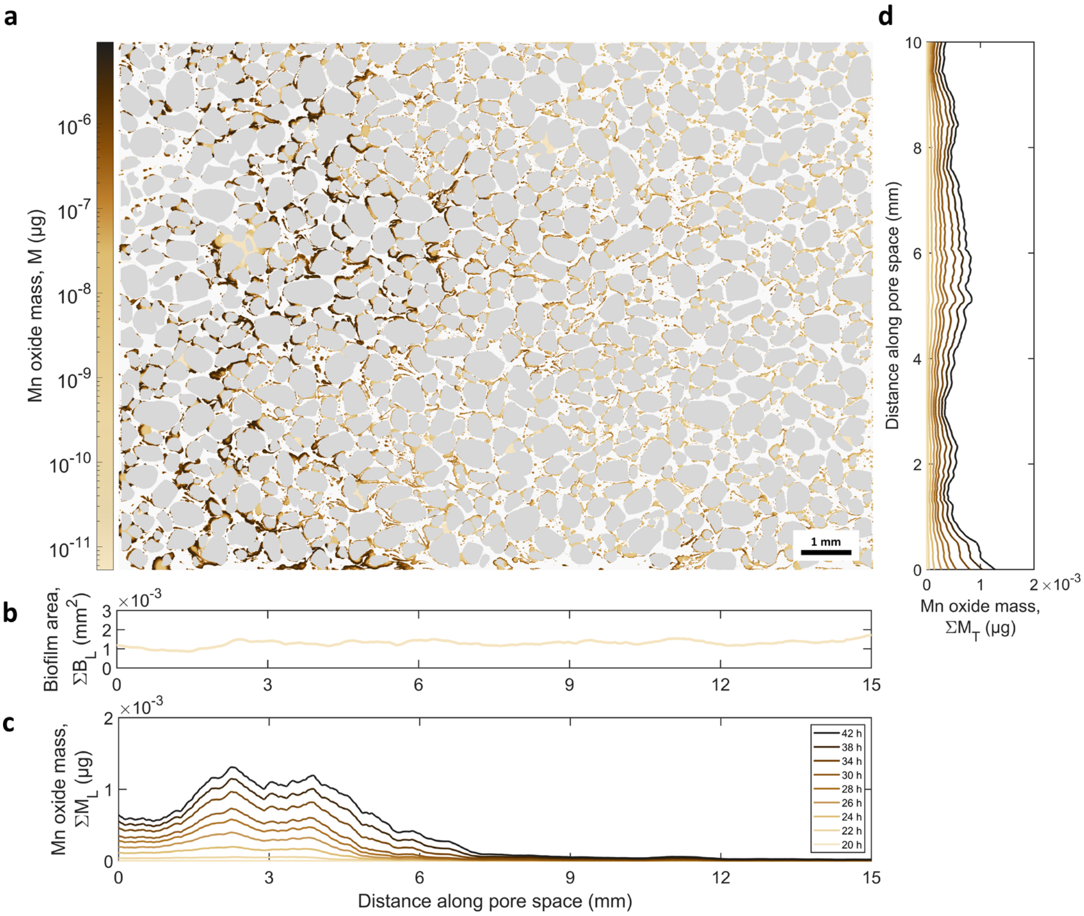

Figure 3. Reactor-scale distribution of Mn oxide mass. One representative experimental replicate is shown here. (a) Mn oxide mass (M) at the end of the mineralization phase (t = 43.5 h). (b) One-dimensional signal of biofilm distribution along the longitudinal direction of flow (ΣB_L) at t = 18.5 h (reference time point). (c) One-dimensional signal of mineral distribution along the longitudinal direction of flow (ΣM_L) at select time points during the mineralization phase. (d) One-dimensional signal of mineral distribution along the transverse direction of flow (ΣM_T) at select time points (see legend in (c)) during the mineralization phase. The one-dimensional signals represent a 1-mm moving average.

increase in effluent Mn(II) between t = 18 h and t = 19 h (Figure 2a) is consistent with Mn(II) desorption, which can occur concomitantly with changes in cell morphology or surface chemistry as bacteria transition to stationary phase.[47,48] Notwithstanding this small release of Mn(II), sorption during the growth phase primed biofilms with Mn(II) that could be rapidly converted to Mn(III, IV) oxides following gene activation and Mn oxidase synthesis at stationary phase.[49] In fact, we observed the rapid removal of Mn(II) from t = 20 to t = 22 h and sustained removal after t = 22 h due to oxidation of Mn(II) to Mn(III, IV) oxides (Figure 2a,b).

3.2. Spatial Distribution of Mn Oxide Precipitation at the Reactor-Scale. As the mineralization phase progressed, a gradient in Mn oxide mass developed along the length of the pore space (Figures 3a, S10a and S11a), as evidenced by the appearance of dark to light brown precipitates (Figures 1d and S7c). Manganese oxide mass decreased from the reactor inlet to the outlet independent of the biofilm distribution, which was largely uniform in the longitudinal direction (Figures 3b, S10b and S11b). We observed that Mn oxides precipitated near the inlet side of the pore space from t = 22 h onward, with most of the mineral mass accumulating in the first half of the pore space in the longitudinal direction of fluid flow (Figures 3c, S10c and S11c). This region of high Mn oxide mass occupied the first ~6 mm, or 40%, of the pore space, extending up to 9 mm (60%) for one replicate, consistent with substantial Mn removal in the top ~40−60% of column-scale sand biofilters.[27,28,30] The lower biofilm area and associated Mn mass at the inlet edge of the pore space was likely due to the UVC irridation of the inlet region. In the transverse direction, oxide distribution was uniform (Figures 3d, S10d and S11d), which confirmed the absence of substantial boundary effects from the reactor geometry.

The observed longitudinal gradient in mineral mass is unlikely to result from external chemical conditions, such as pH or oxygen availability. Although these parameters can influence Mn oxidation,[50] it is unlikely that they were limiting in our system. We provided pH-buffered and oxygen-saturated pore fluid, decreasing the likelihood that mineralization near the reactor outlet would be restricted by unfavorable pH conditions or insufficient oxygen. Additionally, we used PDMS for reactor fabrication, which has been shown to be readily permeable to oxygen.[51,52] Rather than changes in pH or oxygen availability, we expect that the longitudinal mineral gradient develops from the proximity of biofilms at the reactor inlet to the influent Mn(II) source.

Our in situ and real-time analyses elucidate how a gradient in Mn oxide mass develops over time. While initial Mn oxidation occurred throughout the entire pore space, our data show that nascent Mn oxides close to the reactor inlet catalyzed further Mn oxidation, leading to elevated Mn oxide mass. Even though biofilms at the inlet boundary of the pore space experienced a constant concentration of 49.63 ± 0.51 μM Mn(II) during the mineralization phase (Table S2), >95% removal in the reactor effluent indicated a drawdown of Mn(II) along the reactor length, restricting the availability of Mn(II) for downstream biofilms. Over time, enhanced reactivity near the reactor inlet created a positive feedback loop that reinforced spatial heterogeneity and localized mineral accumulation, as evidenced by the Mn oxide mass profiles intensifying over time (Figures 3c, S10c and S11c).

3.3. Limited Diffusion of Mn(II) into Biofilms Enhances Mineralization at Biofilm–Fluid Interfaces.

The reactor-scale gradient in Mn oxide mass (Figures 3a,c, S10a,c and S11a,c) resulted from extensive mineral precipitation at biofilm–fluid interfaces near the reactor inlet. These precipitates formed feathery or dendritic structures at the edges of dense biofilms (Figures 1d and S12). Images acquired with a 40× objective (0.16 μm pixel^{-1}) at the final experimental time point showed that these mineral precipitates contained little fluorescence signal and therefore few embedded cells or cell aggregates (Figure S12). To quantify the accumulation of Mn oxide mass at the biofilm-scale from our time-lapse images, we analyzed transects of representative biofilm–mineral assemblages at multiple time points. These transects extended from the grain–biofilm boundary to the edges of the mineral precipitates that propagated outward from the interface between biofilms and bulk pore fluid (Figures 4a, S13, and Supporting Information Method S7).

Our biofilm-scale analysis confirmed that Mn oxides always precipitated within or adjacent to biofilms, initially accumulating inside biofilms throughout the pore space. However, the mineral mass propagated rapidly outside the footprint of biofilms near the inlet, where Mn(II) entered the reactor, increasing both the area occupied by mineral precipitates and the mass within that area (Figures 4b and S13a). By contrast, minimal Mn oxide mass accumulated in the outlet region far from the Mn(II) source (Figures 4c and S13b). Collectively, biofilms in the first 60% of the pore space (0–9 mm) accumulated ∼30 times more Mn oxide mass outside their footprint than biofilms in the remaining 40% of the pore space (9–15 mm) (Figure S14). Together, these data suggest that interactions between Mn(II) and Mn oxides promote additional mineral precipitation.

Across the entire pore space, Mn oxide mass accumulation shifted from the interior to the exterior of the biofilm footprint over time. As quantified above, biofilms sorbed a total of 0.57 ± 0.16 μg Mn during the first 19 h of the experiment, which facilitated initial Mn oxide precipitation (from approximately t = 19 h to t = 28 h) inside the biofilm footprint (Figure 5a). At the final experimental time point, 1.37 ± 0.09 μg Mn was contained within the biofilm footprint (Figure S14). Assuming all the Mn sorbed prior to t = 19 h was oxidized to Mn oxide, initial Mn(II) sorption accounted for 40.89 ± 9.00% of the total Mn oxide mass on biofilm interiors. At around 29 h, the mineral mass was distributed approximately equally inside and outside the biofilms. At all subsequent time points, more than 50% of the total Mn oxide mass precipitated exterior to the original biofilm footprint. By t = 43.5 h, ∼64% of the total 3.78 ± 0.05 μg Mn oxide mass was outside of the biofilms (Figure 5a), extending the overall projected area of biofilm–mineral assemblages by ∼34% relative to the initial biofilm footprint (Figure S15).

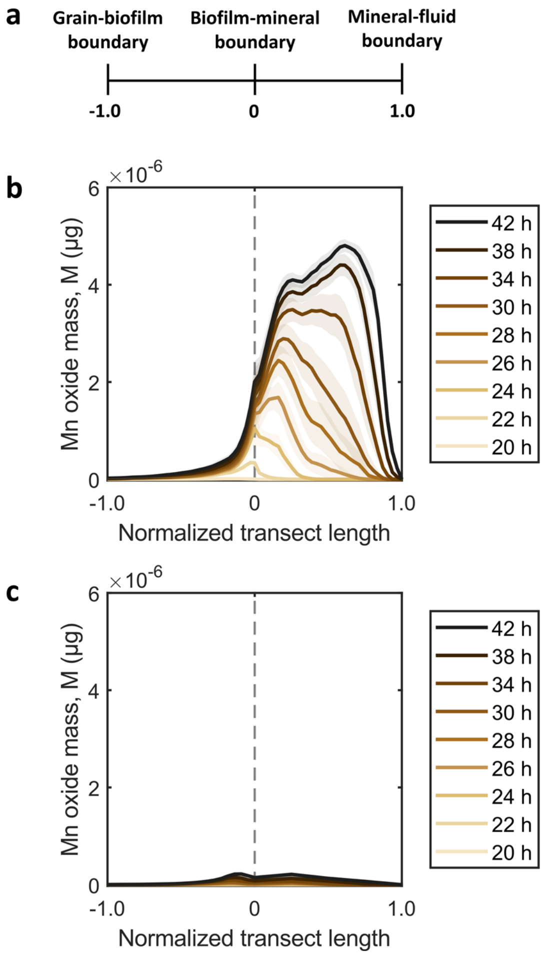

Figure 4. Local distribution of Mn oxide mass inside and outside the biofilm footprint. (a) Schematic of the data normalization strategy, where −1.0 represents the grain–biofilm boundary, 0 represents the biofilm–mineral boundary (dashed line in (b) and (c)), and 1.0 represents the mineral–fluid boundary at the final experimental time point. (b) Mineral mass distribution (M) on biofilms from the inlet side of the reactor (defined as the vertical section of the pore space from 3 to 6 mm or 20 to 40%) at select time points. (c) Mineral mass distribution (M) on biofilms from the outlet side of the reactor (defined as the vertical section of the pore space between 9 to 12 mm or 60 to 80%) at select time points. Solid lines indicate the average mass of nine biofilms, where three biofilms were selected from each replicate experiment, and shading indicates the standard error.

The distribution of mineral mass inside and outside the biofilm footprint can be rationalized by diffusion-limited transport of Mn(II) into the biofilms, resulting from interactions between Mn(II) and Mn oxides. Consistent with enzymatic Mn(II) oxidation, Mn oxide precipitation initially occurred within the biofilms (Figure 4b). With time, these nascent biogenic Mn oxides, especially those nearest to the biofilm–fluid interface, were available to sorb and oxidize Mn(II),[53,54] drawing down the supply of Mn(II) before it could be transported from the biofilm–fluid interface toward the biofilm–grain boundary. We propose that surface-mediated Mn(II) oxidation restricted Mn(II) diffusion from the bulk pore fluid into the biofilms, which limited further Mn oxide mass accumulation within the biofilm footprint (Figure 5a) and generated a reactive and increasingly dense mineral barrier at the biofilm–fluid interface (Figure 4b).

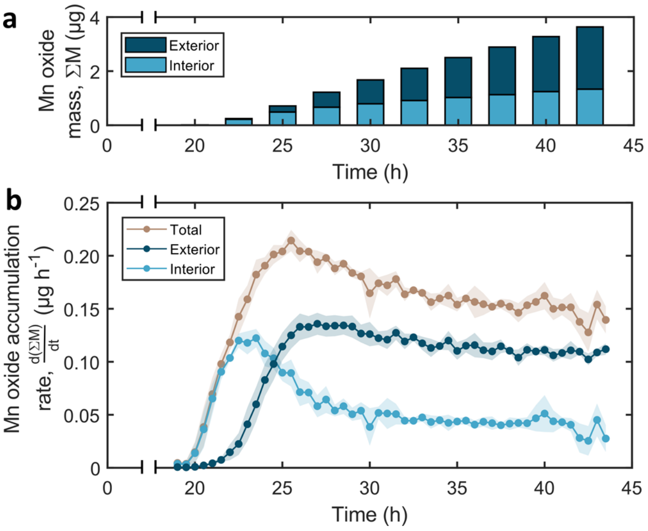

Figure 5. Extent and rate of Mn oxide precipitation inside and outside the biofilm footprint at the reactor-scale. (a) Mn oxide mass accumulation (ΣM) on biofilm interiors and exteriors at discrete time points during the mineralization phase, shown as the average of experimental triplicates. (b) Rates of Mn oxide accumulation $\left(\frac{d(\Sigma M)}{dt}\right)$ in all biofilm−mineral assemblages (brown), biofilm interiors (light blue), and biofilm exteriors (dark blue). Markers represent the average of triplicate experiments, and shading indicates the standard deviation.

3.4. Rates of Mn Oxide Accumulation Reveal Coupled Precipitation Mechanisms.

The global rate of Mn oxide precipitation for all biofilm−mineral assemblages was driven by spatially distinct processes that were offset in time. The global rate of mineral precipitation, calculated as the derivative of Mn oxide mass accumulation between consecutive time points, was non-monotonic (Figure 5b), initially increasing rapidly and peaking at t = 25.5 h (maximum rate of 0.21 ± 0.01 μg h^{-1}) before decelerating gradually to 0.14 ± 0.01 μg h^{-1} at t = 43.5 h. At the onset of detectable Mn oxide precipitation (t = 19 h to t = 21.5 h), the global rate was driven entirely by mineral accumulation inside the biofilms, which we attribute to enzymatic Mn(II) oxidation. The interior mineralization rate reached a maximum at t = 23.5 h (0.12 ± 0.01 μg h^{-1}). After this time, we observed an appreciable increase in the rate of mineral accumulation outside the biofilm footprint. This exterior rate increased from t = 21.5 h until t = 27 h (0.14 ± 0.01 μg h^{-1}), after which it also decelerated. Nonetheless, during the remainder of the experiment (t > 27 h), the global rate of mineral accumulation was sustained by surface-mediated Mn oxide precipitation exterior to the biofilm footprint.

The dominant contribution of the exterior rate to the global kinetics (Figure 5b) was more apparent when we compared the rates on a per-area basis (Figure S16). For precipitation inside the biofilm footprint, we normalized the change in mineral mass between consecutive time points (μg h^{-1}) by the area (mm^2) of all biofilms in the pore space. For precipitation outside the biofilm footprint, we normalized the change in mass by the change in mineral area exterior to the biofilms from the preceding time point to capture the effect of reactivity between nascent oxides and Mn(II). This approach showed that the area-normalized rate was up to 2 orders of magnitude higher outside the biofilm footprint than inside (Figure S16) and explains the large mineral mass exterior to the biofilms (Figure 5a). Nonetheless, the temporal offset of 3.5 h in maximum Mn oxide accumulation rates inside and outside the biofilm footprint, resulting from the concurrent decrease in the interior rate and increase in the exterior rate (Figure 5b), shows unequivocally that enzymatic oxidation is a prerequisite for any subsequent abiotic oxidation outside biofilms. These findings corroborate the tight coupling between biotic and abiotic mineralization processes in porous environments.

3.5. Toward a Conceptual Model of Pore-Scale Mn (Bio)mineralization.

In this study, we demonstrate that Mn oxide mass became elevated close to the Mn(II) source due to enhanced reactivity at the biofilm−fluid interface. Mineral accumulation outside the initial biofilm footprint occurred at higher rates and accounted for the majority of Mn oxide mass within the pore space over long time scales. Based on our in situ quantification, as well as ex situ measurements of Mn(II) removal from the reactor effluent, we propose a conceptual model for Mn oxide precipitation in porous media. Our model integrates five key steps: (i) Mn(II) sorption by developing biofilms, (ii) enzymatic Mn(II) oxidation and precipitation following Mn oxidase synthesis by *P. putida* GB-1 at stationary phase, (iii) continued oxidation of influent Mn(II) by both *P. putida* GB-1 and nascent biogenic Mn oxides, (iv) diffusion-limited transport of Mn(II) and restriction of enzymatic oxidation as minerals in contact with the bulk pore fluid progressively shield bacteria from Mn(II), and (v) enhanced surface-mediated oxidation at the biofilm−fluid interface, which sustains mineral accumulation outside of the biofilm footprint.

3.6. Implications for Porous Media.

Manganese biomineralization drives a range of biogeochemical processes in porous media, from carbon cycling[1,2,4] and metal immobilization[1,2,10] in soils and sediments to Mn(II) removal[27−32] in water treatment systems. However, quantification of Mn oxide precipitation dynamics within these complex environments has largely been limited to pore water analysis and destructive sampling. Our work showcases the opportunities provided by microfluidic systems to quantify in situ biogeochemical reactions at multiple scales (e.g., pore space and individual biofilms) and in real time, allowing us to provide a mechanistic explanation for upscaled observations of oxidative processes and mineral distribution.[27−30,32]

In this study, we observed that mineral accumulation evolved in time and space due to coupled biotic and abiotic processes. The contribution of abiotic processes to continued mineral accumulation (Figures 3, 4, and 5) has substantial implications for engineered treatment systems. While abiotic oxidation can enhance Mn oxide formation and help sustain precipitation rates beyond what biotic processes alone can achieve, mineral propagation into the pore space (Figure S15) may eventually lead to clogging that decreases treatment efficiency over long operational time scales. Future work may investigate how tuning the system hydrodynamics can change the biofilm distribution to mitigate blockages from mineral precipitation while maximizing the porous domain used for Mn(II) removal. Biotic and abiotic mechanisms of Mn oxide precipitation also dictate mineral structure and reactivity. While biogenic Mn oxides are predominantly Mn(IV), abiotic processes can increase the oxide's solid-phase Mn(III) content.[17,18,53,54] During surface-mediated oxidation, aqueous Mn(II) sorbs to Mn oxide particles, transferring electrons to Mn(IV) and remaining as sorbed or incorporated Mn(III).

Consequently, continued exposure to Mn(II) influences mineral reactivity toward organic and inorganic species.[6,11,18,53−56]

Our optical imaging approach allows us to quantify distinct mineral precipitation processes but does not provide chemical information. Direct measurement of Mn speciation, which could be achieved with synchrotron-based X-ray spectroscopy, would confirm that Mn oxide accumulation at biofilm−fluid interfaces results from abiotic oxidation processes, allowing us to explore how mineral reactivity toward Mn(II) and co-occurring contaminants would evolve over time. Though it has not been explicitly documented for Mn biomineralization, extracellular polymers at the biofilm−fluid interface may also promote Mn precipitation by increasing the local concentrations of Mn(II) or modulating the interfacial energy associated with mineral nucleation.[57−60] Future research should focus on integrating spectroscopy and microfluidic systems to further define the contribution of microbes, mineral surfaces, and EPS to Mn(II) removal and Mn oxide precipitation in porous media.

While we investigated Mn oxide precipitation under specific experimental parameters (fixed flow rate, defined fluid chemistry, model bacterium), pore-scale biomineralization is inherently dynamic and heterogeneous.[22] For instance, both soils and treatment systems experience transient flow, such as water table fluctuations or filter backwash, that influences biofilm attachment and spatial localization of mineral precipitates. Pore fluids also have variable ionic strength, redox potential, and pH, all of which dictate the kinetics of mineral nucleation and precipitation. Finally, porous media host diverse microbial communities, whose interactions control resource allocation, biofilm development, and the resulting distribution and stability of mineral precipitates. By establishing a framework for quantifying in situ biogeochemical transformations in porous media analogs, our study creates opportunities to bridge the gap between mechanistic pore-scale experiments, column systems, and complex natural environments.

ASSOCIATED CONTENT

Data Availability Statement

All data and codes associated with this work can be found on the Dryad data repository at DOI: 10.5061/dryad.sj3tx96gx. Any additional requests can be addressed to the corresponding author.

Supporting Information

The Supporting Information is available free of charge at https://pubs.acs.org/doi/10.1021/acs.est.5c11326.

> Details on batch growth characterization, microfluidic reactor design, setup of the microfluidic flow control system, components and operation of the UVC sample stage; detailed mass balance calculations and summary of mass closure results; description of color calibration and image analysis workflow; 4× fluorescence and color brightfield images of *P. putida* GB-1 biofilms in the reactor pore space; 4× images and binary masks showing delineation of the biofilm footprint; replicate analysis of Mn oxide spatial distribution at the reactor-scale; 40× fluorescence and color brightfield images of biofilms and exterior Mn oxide accumulation; replicate analysis of Mn oxide spatial distribution at the biofilm-scale; and analysis of the mass, spatial extent, and area-normalized rate of mineral accumulation inside and outside the biofilm footprint (PDF)

AUTHOR INFORMATION

Corresponding Author

Jasquelin Peña − *Department of Civil and Environmental Engineering, University of California Davis, Davis, California 95616, United States; Energy Geosciences Division, Earth and Environmental Sciences Area, Lawrence Berkeley National Laboratory, Berkeley, California 94720, United States;* orcid.org/0000-0001-7081-3873; Email: pena@ucdavis.edu

Authors

Eleanor C. Fadely − *Department of Civil and Environmental Engineering, University of California Davis, Davis, California 95616, United States*

Gaitan Gehin − *Department of Civil and Environmental Engineering, University of California Davis, Davis, California 95616, United States*

Sharon E. Bone − *Institute of Bio- and Geosciences: Agrosphere, Forschungszentrum Jülich, Jülich 52428, Germany;* orcid.org/0000-0002-7521-9627

Samuel M. Webb − *Stanford Synchrotron Radiation Lightsource, SLAC National Accelerator Laboratory, Menlo Park, California 94025, United States*

Verónica L. Morales − *Department of Civil and Environmental Engineering, University of California Davis, Davis, California 95616, United States;* orcid.org/0000-0002-9595-6026

Complete contact information is available at: https://pubs.acs.org/10.1021/acs.est.5c11326

Author Contributions

E.C.F., G.G., V.L.M., and J.P. designed the research. E.C.F. performed the research and wrote the image analysis scripts. S.E.B. and S.M.W. contributed to X-ray fluorescence-based image calibration. E.C.F., G.G., V.L.M., and J.P. analyzed the data and wrote the manuscript.

Notes

The authors declare no competing financial interest.

ACKNOWLEDGMENTS

This project was supported by the U.S. National Science Foundation Center for Bio-mediated and Bio-inspired Geotechnics (ERC-1449501) and a U.S. Department of Energy Office of Science Graduate Student Research (SCGSR) award to E.C.F. We also acknowledge the support of the Swiss National Science Foundation (200021_188546) and the U.S. National Science Foundation, including MCA-2322428, EAR-1847689, and the SEES: Synchrotron Earth and Environmental Science Program (EAR-2223273). Part of this study was carried out at the UC Davis Center for Nano and Micro Manufacturing (CNM2). Use of the Stanford Synchrotron Radiation Lightsource, SLAC National Accelerator Laboratory, is supported by the U.S. Department of Energy, Office of Science, Office of Basic Energy Sciences under Contract No. DE-AC02-76SF00515. We thank Vladimir Sentchilo and Jan Roelof van der Meer for the construction of the constitutive fluorescent-tagged *P. putida* GB-1 strain. We also thank Yuze Wang and Jason DeJong for sharing the porous medium geometry used for microfluidic reactor fabrication. We acknowledge Steven Lucero and the UC Davis Tech Foundry for design and fabrication of the microscope incubator and UVC sample stage. Finally, we acknowledge the Seker Lab for training on photolithography and soft lithography, Sharod Nandi and Kyounglim Kang for their assistance with effluent sample collection and ICP-MS analysis, Filippo Miele for helpful discussions on image segmentation, and Lotus Ufondu for batch microbial strain characterization.

REFERENCES

(1) Hansel, C. M.; Learman, D. R. Geomicrobiology of Manganese. In *Ehrlich's Geomicrobiology*; Ehrlich, H. L., Newman, D. K., Kappler, A., Eds.; CRC Press, 2015.

(2) Tebo, B. M.; Bargar, J. R.; Clement, B. G.; Dick, G. J.; Murray, K. J.; Parker, D.; Verity, R.; Webb, S. M. Biogenic Manganese Oxides: Properties and Mechanisms of Formation. *Annu. Rev. Earth Planet. Sci.* **2004**, *32* (1), 287−328.

(3) Tebo, B. M.; Johnson, H. A.; McCarthy, J. K.; Templeton, A. S. Geomicrobiology of Manganese(II) Oxidation. *Trends Microbiol.* **2005**, *13* (9), 421−428.

(4) Li, H.; Santos, F.; Butler, K.; Herndon, E. A Critical Review on the Multiple Roles of Manganese in Stabilizing and Destabilizing Soil Organic Matter. *Environ. Sci. Technol.* **2021**, *55* (18), 12136−12152.

(5) Droz, B.; Dumas, N.; Duckworth, O. W.; Peña, J. A Comparison of the Sorption Reactivity of Bacteriogenic and Mycogenic Mn Oxide Nanoparticles. *Environ. Sci. Technol.* **2015**, *49* (7), 4200−4208.

(6) Holguera, J. G.; Etui, I. D.; Jensen, L. H. S.; Peña, J. Contaminant Loading and Competitive Access of Pb, Zn and Mn(III) to Vacancy Sites in Biogenic MnO2. *Chem. Geol.* **2018**, *502*, 76−87.

(7) Peña, J.; Kwon, K. D.; Refson, K.; Bargar, J. R.; Sposito, G. Mechanisms of Nickel Sorption by a Bacteriogenic Birnessite. *Geochim. Cosmochim. Acta* **2010**, *74* (11), 3076−3089.

(8) Toner, B.; Manceau, A.; Webb, S. M.; Sposito, G. Zinc Sorption to Biogenic Hexagonal-Birnessite Particles within a Hydrated Bacterial Biofilm. *Geochim. Cosmochim. Acta* **2006**, *70* (1), 27−43.

(9) Villalobos, M.; Bargar, J.; Sposito, G. Mechanisms of Pb(II) Sorption on a Biogenic Manganese Oxide. *Environ. Sci. Technol.* **2005**, *39* (2), 569−576.

(10) Grangeon, S.; Bataillard, P.; Coussy, S. The Nature of Manganese Oxides in Soils and Their Role as Scavengers of Trace Elements: Implication for Soil Remediation. In *Environmental Soil Remediation and Rehabilitation*; van Hullebusch, E. D., Huguenot, D., Pechaud, Y., Simonnot, M.-O., Colombano, S., Eds.; *Applied Environmental Science and Engineering for a Sustainable Future*; Springer International Publishing: Cham, 2020; pp 399−429.

(11) Remucal, C. K.; Ginder-Vogel, M. A Critical Review of the Reactivity of Manganese Oxides with Organic Contaminants. *Environ. Sci.: Processes Impacts* **2014**, *16* (6), 1247.

(12) Chaput, D. L.; Hansel, C. M.; Burgos, W. D.; Santelli, C. M. Profiling Microbial Communities in Manganese Remediation Systems Treating Coal Mine Drainage. *Appl. Environ. Microbiol.* **2015**, *81* (6), 2189−2198.

(13) Duckworth, O. W.; Rivera, N. A.; Gardner, T. G.; Andrews, M. Y.; Santelli, C. M.; Polizzotto, M. L. Morphology, Structure, and Metal Binding Mechanisms of Biogenic Manganese Oxides in a Superfund Site Treatment System. *Environ. Sci.: Processes Impacts* **2017**, *19* (1), 50−58.

(14) Piazza, A.; Ciancio Casalini, L.; Pacini, V. A.; Sanguinetti, G.; Ottado, J.; Gottig, N. Environmental Bacteria Involved in Manganese-(II) Oxidation and Removal From Groundwater. *Front. Microbiol.* **2019**, *10*, 119.

(15) Peña, J.; Bargar, J. R.; Sposito, G. Role of Bacterial Biomass in the Sorption of Ni by Biomass-Birnessite Assemblages. *Environ. Sci. Technol.* **2011**, *45* (17), 7338−7344.

(16) Toner, B.; Fakra, S.; Villalobos, M.; Warwick, T.; Sposito, G. Spatially Resolved Characterization of Biogenic Manganese Oxide Production within a Bacterial Biofilm. *Appl. Environ. Microbiol.* **2005**, *71* (3), 1300−1310.

(17) Bargar, J. R.; Tebo, B. M.; Bergmann, U.; Webb, S. M.; Glatzel, P.; Chiu, V. Q.; Villalobos, M. Biotic and Abiotic Products of Mn(II) Oxidation by Spores of the Marine *Bacillus Sp.* Strain SG-1. *Am. Mineral.* **2005**, *90* (1), 143−154.

(18) Learman, D. R.; Wankel, S. D.; Webb, S. M.; Martinez, N.; Madden, A. S.; Hansel, C. M. Coupled Biotic−Abiotic Mn(II) Oxidation Pathway Mediates the Formation and Structural Evolution of Biogenic Mn Oxides. *Geochim. Cosmochim. Acta* **2011**, *75* (20), 6048−6063.

(19) Gerke, H. H. Preferential Flow Descriptions for Structured Soils. *Z. Pflanzenernähr. Bodenk.* **2006**, *169* (3), 382−400.

(20) Dentz, M.; Le Borgne, T.; Englert, A.; Bijeljic, B. Mixing, Spreading and Reaction in Heterogeneous Media: A Brief Review. *J. Contam. Hydrol.* **2011**, *120−121*, 1−17.

(21) Kleber, M.; Bourg, I. C.; Coward, E. K.; Hansel, C. M.; Myneni, S. C. B.; Nunan, N. Dynamic Interactions at the Mineral−Organic Matter Interface. *Nat. Rev. Earth Environ.* **2021**, *2* (6), 402−421.

(22) Jimenez-Martinez, J.; Nguyen, J.; Or, D. Controlling Pore-Scale Processes to Tame Subsurface Biomineralization. *Rev. Environ. Sci. Biotechnol.* **2022**, *21* (1), 27−52.

(23) Or, D.; Smets, B. F.; Wraith, J. M.; Dechesne, A.; Friedman, S. P. Physical Constraints Affecting Bacterial Habitats and Activity in Unsaturated Porous Media − a Review. *Adv. Water Resour.* **2007**, *30* (6−7), 1505−1527.

(24) Post, J. E. Manganese Oxide Minerals: Crystal Structures and Economic and Environmental Significance. *Proc. Natl. Acad. Sci. U.S.A.* **1999**, *96* (7), 3447−3454.

(25) Farnsworth, C. E.; Voegelin, A.; Hering, J. G. Manganese Oxidation Induced by Water Table Fluctuations in a Sand Column. *Environ. Sci. Technol.* **2012**, *46* (1), 277−284.

(26) Robbins, E. I.; Corley, T. L. Microdynamics and Seasonal Changes in Manganese Oxide Epiprecipitation in Pinal Creek, Arizona. *Hydrobiologia* **2005**, *534* (1), 165−180.

(27) Li, C.; Wang, S.; Du, X.; Cheng, X.; Fu, M.; Hou, N.; Li, D. Immobilization of Iron- and Manganese-Oxidizing Bacteria with a Biofilm-Forming Bacterium for the Effective Removal of Iron and Manganese from Groundwater. *Bioresour. Technol.* **2016**, *220*, 76−84.

(28) Haukelidsaeter, S.; Boersma, A. S.; Piso, L.; Lenstra, W. K.; van Helmond, N. A. G. M.; Schoonenberg, F.; van der Pol, E.; Hurtarte, L. C. C.; van der Wielen, P. W. J. J.; Behrends, T.; van Kessel, M. A. H. J.; Lücker, S.; Slomp, C. P. Efficient Chemical and Microbial Removal of Iron and Manganese in a Rapid Sand Filter and Impact of Regular Backwash. *Appl. Geochem.* **2024**, *162*, 105904.

(29) Bruins, J. H.; Petrusevski, B.; Slokar, Y. M.; Huysman, K.; Joris, K.; Kruithof, J. C.; Kennedy, M. D. Biological and Physico-Chemical Formation of Birnessite during the Ripening of Manganese Removal Filters. *Water Res.* **2015**, *69*, 154−161.

(30) Breda, I. L.; Søborg, D. A.; Ramsay, L.; Roslev, P. Manganese Removal Processes during Start-up of Inoculated and Non-Inoculated Drinking Water Biofilters. *Water Qual. Res. J.* **2019**, *54* (1), 47−56.

(31) Hallberg, K. B.; Johnson, D. B. Biological Manganese Removal from Acid Mine Drainage in Constructed Wetlands and Prototype Bioreactors. *Sci. Total Environ.* **2005**, *338* (1−2), 115−124.

(32) Wang, R.; Hu, H.; Shi, D.; Liang, J.; Shao, S. Mechanism of Mn(II) Removal by the Cake Layer Containing Biogenic Manganese Oxides in a Flow-through Mode: Biological or Chemical Catalysis? *Sep. Purif. Technol.* **2024**, *330*, 125214.

(33) Gehin, G.; Carraro, N.; van der Meer, J. R.; Peña, J. Population-Level Control of Two Manganese Oxidases Expands the Niche for Bacterial Manganese Biomineralization. *npj Biofilms Microbiomes* **2025**, *11* (1), 1−12.

(34) Geszvain, K.; McCarthy, J. K.; Tebo, B. M. Elimination of Manganese(II,III) Oxidation in Pseudomonas Putida GB-1 by a Double Knockout of Two Putative Multicopper Oxidase Genes. *Appl. Environ. Microbiol.* **2013**, *79* (1), 357−366.

(35) Santelli, C. M.; Pfister, D. H.; Lazarus, D.; Sun, L.; Burgos, W. D.; Hansel, C. M. Promotion of Mn(II) Oxidation and Remediation

of Coal Mine Drainage in Passive Treatment Systems by Diverse Fungal and Bacterial Communities. *Appl. Environ. Microbiol.* **2010**, *76* (14), 4871−4875.

(36) Flemming, H.-C.; Wingender, J. The Biofilm Matrix. *Nat. Rev. Microbiol.* **2010**, *8* (9), 623−633.

(37) Wang, Y.; Soga, K.; Dejong, J. T.; Kabla, A. J. A Microfluidic Chip and Its Use in Characterising the Particle-Scale Behaviour of Microbial-Induced Calcium Carbonate Precipitation (MICP). *Géotechnique* **2019**, *69* (12), 1086−1094.

(38) Ramos, G.; Toulouze, C.; Rima, M.; Liot, O.; Duru, P.; Davit, Y. Ultraviolet Control of Bacterial Biofilms in Microfluidic Chips. *Biomicrofluidics* **2023**, *17* (2), 024107.

(39) Hein, C.; Sander, J. M.; Kautenburger, R. New Approach of a Transient ICP-MS Measurement Method for Samples with High Salinity. *Talanta* **2017**, *164*, 477−482.

(40) Schlechter, R. O.; Kear, E. J.; Remus, D. M.; Remus-Emsermann, M. N. P. Fluorescent Protein Expression as a Proxy for Bacterial Fitness in a High-Throughput Assay. *Appl. Environ. Microbiol.* **2021**, *87* (18), No. e0098221.

(41) Fein, J. B.; Yu, Q.; Nam, J.; Yee, N. Bacterial Cell Envelope and Extracellular Sulfhydryl Binding Sites: Their Roles in Metal Binding and Bioavailability. *Chem. Geol.* **2019**, *521*, 28−38.

(42) Li, C.; Yu, Y.; Fang, A.; Feng, D.; Du, M.; Tang, A.; Chen, S.; Li, A. Insight into Biosorption of Heavy Metals by Extracellular Polymer Substances and the Improvement of the Efficacy: A Review. *Lett. Appl. Microbiol.* **2022**, *75* (5), 1064−1073.

(43) Toner, B.; Manceau, A.; Marcus, M. A.; Millet, D. B.; Sposito, G. Zinc Sorption by a Bacterial Biofilm. *Environ. Sci. Technol.* **2005**, *39* (21), 8288−8294.

(44) Tourney, J.; Ngwenya, B. T. The Role of Bacterial Extracellular Polymeric Substances in Geomicrobiology. *Chem. Geol.* **2014**, *386*, 115−132.

(45) Vázquez-Ortega, A.; Fein, J. B. Thermodynamic Modeling of Mn(II) Adsorption onto Manganese Oxidizing Bacteria. *Chem. Geol.* **2017**, *464*, 147−154.

(46) Banh, A.; Chavez, V.; Doi, J.; Nguyen, A.; Hernandez, S.; Ha, V.; Jimenez, P.; Espinoza, F.; Johnson, H. A. Manganese (Mn) Oxidation Increases Intracellular Mn in Pseudomonas Putida GB-1. *PLoS One* **2013**, *8* (10), No. e77835.

(47) Jaishankar, J.; Srivastava, P. Molecular Basis of Stationary Phase Survival and Applications. *Front. Microbiol.* **2017**, *8*, 2000.

(48) Daughney, C. J.; Fowle, D. A.; Fortin, D. The Effect of Growth Phase on Proton and Metal Adsorption by Bacillus Subtilis. *Geochim. Cosmochim. Acta* **2001**, *65* (7), 1025−1035.

(49) Gehin, G.; Carraro, N.; Gurfield, K.; van der Meer, J. R.; Peña, J. Pseudomonas Putida Coordinates the Expression of Two Manganese Oxidases and Optimizes Manganese Oxide Precipitation in Response to Aqueous Mn(II). *Environ. Sci. Technol.* **2025**, *59* (27), 13777−13786.

(50) Okazaki, M.; Sugita, T.; Shimizu, M.; Ohode, Y.; Iwamoto, K.; de Vrind-de Jong, E. W.; de Vrind, J. P.; Corstjens, P. L. Partial Purification and Characterization of Manganese-Oxidizing Factors of Pseudomonas Fluorescens GB-1. *Appl. Environ. Microbiol.* **1997**, *63*, 4793−4799.

(51) Stern, S. A. Polymers for Gas Separations: The next Decade. *J. Membr. Sci.* **1994**, *94* (1), 1−65.

(52) Markov, D. A.; Lillie, E. M.; Garbett, S. P.; McCawley, L. J. Variation in Diffusion of Gases through PDMS Due to Plasma Surface Treatment and Storage Conditions. *Biomed. Microdevices* **2014**, *16* (1), 91−96.

(53) Elzinga, E. J. Reductive Transformation of Birnessite by Aqueous Mn(II). *Environ. Sci. Technol.* **2011**, *45* (15), 6366−6372.

(54) Zhao, H.; Zhu, M.; Li, W.; Elzinga, E. J.; Villalobos, M.; Liu, F.; Zhang, J.; Feng, X.; Sparks, D. L. Redox Reactions between Mn(II) and Hexagonal Birnessite Change Its Layer Symmetry. *Environ. Sci. Technol.* **2016**, *50* (4), 1750−1758.

(55) Lefkowitz, J. P.; Elzinga, E. J. Structural Alteration of Hexagonal Birnessite by Aqueous Mn(II): Impacts on Ni(II) Sorption. *Chem. Geol.* **2017**, *466*, 524−532.

(56) Simanova, A. A.; Peña, J. Time-Resolved Investigation of Cobalt Oxidation by Mn(III)-Rich δ-MnO2 Using Quick X-Ray Absorption Spectroscopy. *Environ. Sci. Technol.* **2015**, *49* (18), 10867−10876.

(57) Emerson, D.; Fleming, E. J.; McBeth, J. M. Iron-Oxidizing Bacteria: An Environmental and Genomic Perspective. *Annu. Rev. Microbiol.* **2010**, *64* (64), 561−583.

(58) Ehrlich, H.; Bailey, E.; Wysokowski, M.; Jesionowski, T. Forced Biomineralization: A Review. *Biomimetics* **2021**, *6* (3), 46.

(59) Decho, A. W. Overview of Biopolymer-Induced Mineralization: What Goes on in Biofilms? *Ecol. Eng.* **2010**, *36* (2), 137−144.

(60) Gadd, G. M. Metals, Minerals and Microbes: Geomicrobiology and Bioremediation. *Microbiology* **2010**, *156* (3), 609−643.